IEEE Photonics Journal
An IEEE Photonics Society Publication

Open Access

Structural Optimization of Photonic Crystals for Enhancing Optical Absorption of Thin Film Silicon Solar Cell Structures

Volume 6, Number 1, February 2014

Yosuke Kawamoto
Yoshinori Tanaka
Kenji Ishizaki
Menaka De Zoysa
Takashi Asano
Susumu Noda

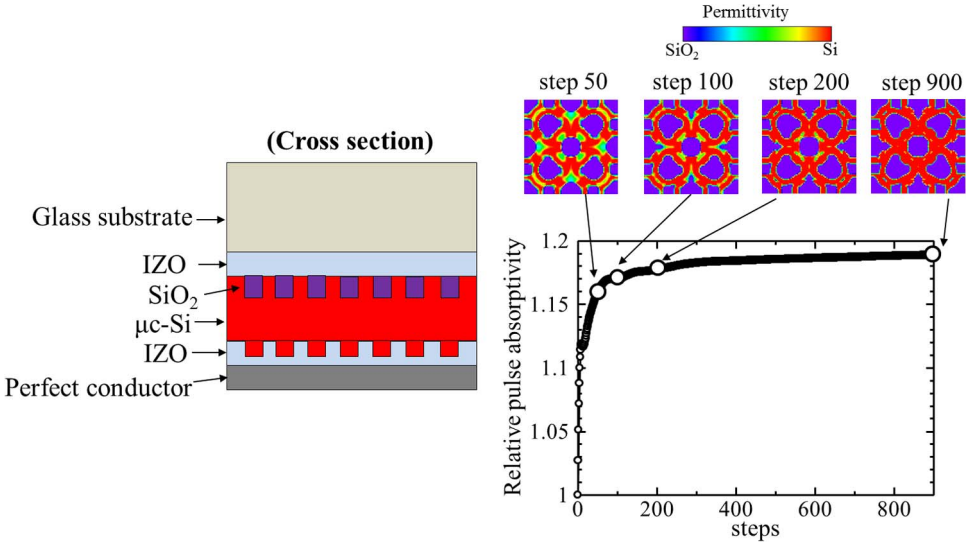

DOI: 10.1109/JPHOT.2014.2302800
1943-0655

IEEE photonics SOCIETY
IEEE

Structural Optimization of Photonic Crystals for Enhancing Optical Absorption of Thin Film Silicon Solar Cell Structures

Yosuke Kawamoto, Yoshinori Tanaka, Kenji Ishizaki, Menaka De Zoysa, Takashi Asano, and Susumu Noda

Department of Electronic Science and Engineering, Kyoto University, Kyoto 615-8510, Japan

DOI: 10.1109/JPHOT.2014.2302800

Manuscript received January 10, 2014; accepted January 15, 2014. Date of publication January 28, 2014; date of current version February 3, 2014. This work was supported in part by the Core Research for Evolutional Science and Technology (CREST) and the Consortium for Photon Science and Technology (C-PhoST) from the Japan Science and Technology Agency (JST) and in part by Grants for Excellent Graduate Schools from the Ministry of Education, Culture, Sports, Science and Technology of Japan. Corresponding author: Y. Kawamoto (e-mail: kawamoto@qoe.kuee.kyoto-u.ac.jp).

Abstract: We carry out the structural design of photonic crystals to enhance the optical absorption of thin-film microcrystalline silicon (μc-Si) solar cells using two methods. First, by exhaustive search, we choose a structure with the largest absorption within the investigated patterns. Then we employ a sensitivity analysis to finely modulate the structure for further increase of the optical absorption. The obtained μc-Si solar cell structure with a photonic crystal in this work has more than twice as much optical absorption as that without a photonic crystal.

Index Terms: Photonic crystal.

Worldwide interest in using solar photovoltaics continues to increase in the world. Silicon (Si) is used in the most widespread solar cells, and among them, crystalline Si solar cells are commonly used, whose thicknesses can be as much as 100–200 μm. Considering the future popularization of solar photovoltaics, the supply of Si resources will become critical. Thin film Si solar cells, whose thicknesses are as small as several hundred nm to several μm, are one candidate to overcome this issue. However, because the optical path length in photovoltaic materials is shorter, thin film Si solar cells have less optical absorption within a wavelength range near the Si electronic band-gap edge, especially 600-1000 nm. To solve this problem, a textured structure is widely used, where photons are trapped by random scattering structure [1]–[3]. However, because of the randomness, the characteristics of each device are different, and the design rule of random structures with large optical absorption is not so clear.

On the other hand, the use of photonic crystals and other methods including microsphere array [4]–[10] has been attracting much attention as a method to extend the interaction time between photons and photovoltaic materials. Various functionalities of photonic crystals have already been shown [7]–[10], and one important characteristic is in-plane resonance with a large area at their band-edge [11]–[13]. This resonance phenomenon occurs at the band-edge of a photonic crystal, where the group velocity of light becomes zero, and light traveling in different directions is coupled to each other. If incident light is coupled to the band-edge resonance mode of a photonic crystal, the interaction time to the Si layer becomes longer, enhancing optical absorption in the Si.

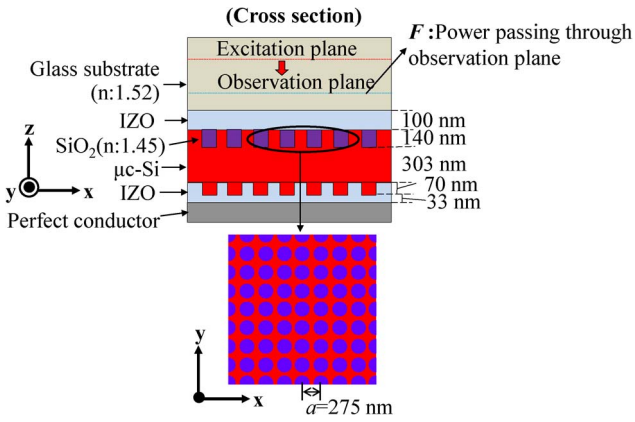

Fig. 1. Schematic of solar cell structure (a photonic crystal is fundamental lattice). Cylindrical silicon dioxide (SiO_2) rods (140 nm height, and lattice constant *a* is 275 nm) are stacked on the indium-doped zinc oxide (IZO) layer on the glass substrate. We assume that on the opposite side, cylindrical μc-Si rods protrude by 70 nm. μc-Si layer thickness is 303 nm, and IZO layer thickness with μc-Si rods is 33 nm.

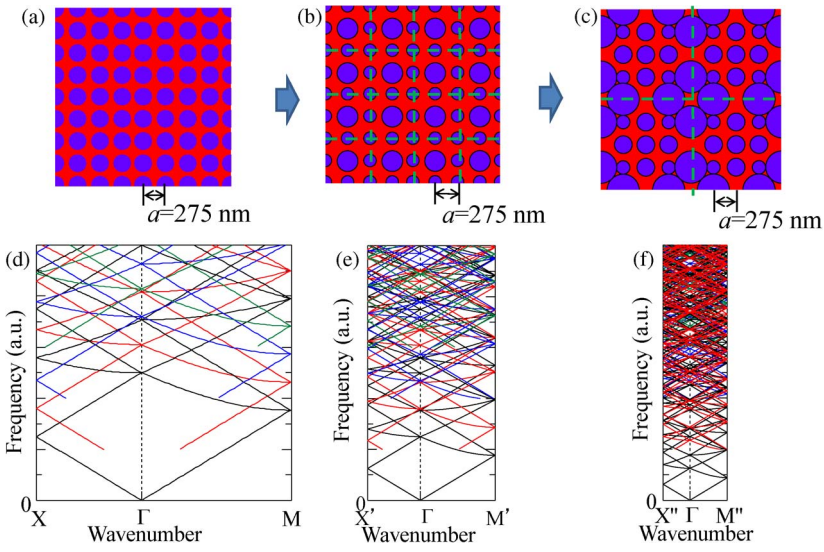

Fig. 2. (a) Real space image of fundamental lattice photonic crystal with lattice constant of *a*. (b) Real space image of 2 $\times$ 2 period photonic superlattice. (c) Real space image of 4 $\times$ 4 period photonic superlattice. (d) Schematic of band diagram for structure shown in Fig. 2(a). (e) Schematic of band diagram for structure shown in Fig. 2(b). (f) Schematic of band diagram for structure shown in Fig. 2(c).

We demonstrated such enhancement of optical absorption by the band-edge effect of photonic crystals for a single wavelength by satisfying *Q* matching condition [14]. When *Q* matching condition is satisfied, the optical absorption to the Si layer is enhanced due to light trapping effects and consequently reflection is reduced. We also recently investigated the structure shown in Fig. 1, where the average thickness of the microcrystalline silicon (μc-Si) layer (400 nm) is larger than the wavelength in the μc-Si of the visible and near infrared light. Therefore, multiple photonic band-edge modes are generated by higher order modes for the vertical direction of the Si layer, which enables enhancement of the optical absorption on multiple wavelengths [15]. We also investigated the employment of the photonic superlattice structures shown in Fig. 2(b) and (c), where multiple lattice points are included in the period while maintaining the periodicity of the original photonic crystal structure [15]. By introducing photonic superlattice structures, the fundamental Brillouin zone size is reduced, and photonic bands are folded in the Γ-point directions. As a result, the band diagrams change from Fig. 2(d) to (e) and (f), and the number of Γ-point photonic band-edge modes

increases. In Ref. [15], we investigated the photonic crystal structures shown in Fig. 2(a)–(c) and concluded the average optical absorptivity increased by employing photonic superlattices. The 4×4 period superlattice in Fig. 2(c) exhibits 58.0% of the average optical absorptivity weighted by solar spectral irradiance in a wavelength range of 500–1000 nm, which is 1.8 times larger than that without photonic crystals [15]. However, as for the photonic superlattice structure, concrete design rules for large optical absorption in a wide wavelength range have not been shown. In this paper we investigated better structural design of photonic superlattice structures using the following two steps. First, by exhaustive-search, we determine the structure with the largest absorption within the investigated patterns, and finely modulate the structure by using sensitivity analysis [16], [17].

The calculation model of the solar cell structure in our study is shown in Fig. 1, except for the in-plane shape of the photonic crystal. A photonic crystal consisting of cylindrical silicon dioxide (SiO_2) rods (140 nm height, lattice constant a is 275 nm) is stacked on the indium-doped zinc oxide (IZO) layer on the glass substrate and formed in a Si layer. We assume that cylindrical μc-Si rods protrude by 70 nm on the opposite side. The Si volume is equivalent to that of 400-nm-thick flat Si. The concrete structural parameters are shown in Fig. 1. Although the typical thickness of a μc-Si layer is one or several micrometers, we employed this thickness to further reduce the material usage and the production cost and for easy carrier extraction. Moreover, we chose IZO as a transparent conductive oxide in this work, but other transparent conductive oxide materials are also applicable, including gallium-doped zinc oxide or indium-doped tin oxide. We explored photonic crystal structures with large optical absorption when light entered this structure from a glass layer by electromagnetic field analysis. In the following investigations, we ignored optical absorption of the IZO and the back reflector for simplicity. We used the three-dimensional finite domain difference (3D FDTD) method for the calculations. As the boundary conditions, we adopted Mur's absorbing boundary condition in the z direction and periodic boundary conditions in the $x - y$ plane. The size of the FDTD cell is 13.75 nm, and the number of cells is 80 in the x and y directions and 140 in the z direction, respectively. The refractive indices of materials and absorption coefficient of μc-Si are referred from the previous works [18], [19].

In the structural design, we used 4×4 period photonic superlattices, where multiple lattice points (4×4 periods) are included in the period while maintaining the periodicity of the original photonic crystal structure. As the first step of the structural design, we explored photonic crystal structures that might have large optical absorption, when the radii of the rods varied by exhaustive-search. We discussed photonic crystal structures with 4-fold rotational symmetry to realize polarization independent characteristics and consequently investigated six kinds of rods when their radii varied [see Fig. 3(a)]. Taking computational resources into account, we considered four values, 0.00 a, 0.15 a, 0.30 a, and 0.45 a as the radius of each rod and enumerated 4096 $(= 4^6)$ kinds of symmetrical structures. We calculated F, which is the power passing through the observation plane in Fig. 1, for all the structures. When there is absorption in the photovoltaic materials, the power, which passes through the observation plane in the opposite direction after reflection, is reduced. In our model, we adopted perfect conductor as the back reflector and ignored the optical absorption of the IZO. Therefore, F is equivalent to the optical absorption of the Si. We set a vertically incident short x-polarized pulse (center wavelength is 800 nm and full width half maximum (FWHM) is about 300 nm) in the glass substrate as an excitation source. Although other wavelengths can be selected as the center wavelength of the pulse, we chose this value because we intended to enhance optical absorption of the μc-Si, especially in a wavelength range of 700–900 nm, where absorption for this structure is about 50% and further absorption enhancement is expected. The material parameters for an 800-nm wavelength were used to calculate this step (as described below, calculations considering material dispersion were also carried out). Although our obtained results are weighted by the pulse spectrum and the material dispersion is not considered in this method, the information from a wavelength range of 650–950 nm, where the optical absorption of the thin film Si was relatively low, was expected to be obtained by one pulse excitation. From the 4096 calculation results, we explored the structure with the largest optical absorption for the short pulse and obtained the photonic crystal structure shown in Fig. 3(b).

Next we calculated the optical absorption characteristics in a wavelength range of 500–1000 nm considering the material dispersion of Si. We set a vertically incident x-polarized continuous wave

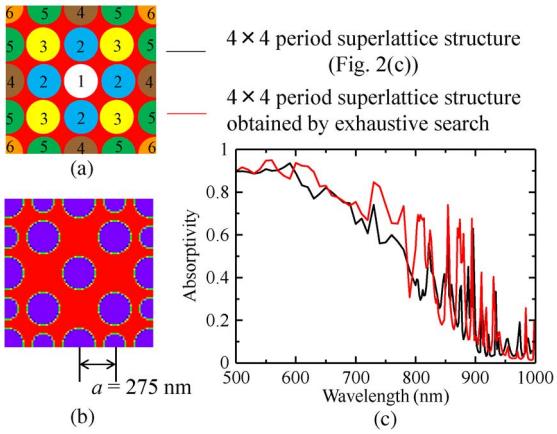

Fig. 3. (a) Schematic of six kinds of rods used in exhaustive-search. Same-colored circles have same radius. (white: rod 1, light blue: rod 2, yellow: rod 3, brown: rod 4, green: rod 5, orange: rod 6). 4-fold rotationally symmetric structure is discussed as shown in this figure. (b) Photonic crystal structure obtained by exhaustive-search (radii of rod 1:0.45 *a*, rod 2: 0.00 *a*, rod 3:0.45 *a*, rod 4:0.45 *a*, rod 5: 0.30 *a*, and rod 6: 0.45 *a*). (c) Optical absorption spectra, obtained by FDTD calculations for 4 × 4 period superlattice shown in Fig. 2(c) and 4 × 4 period superlattice obtained by exhaustive-search [see Fig. (b)].

source in the glass substrate as an excitation source and calculated the optical absorption by the power passing through the observation plane. We also calculated the power for the entire glass structure as a reference and estimated the absorptivity by comparing them. Since the photonic crystal structures mentioned in this paper have 4-fold rotational symmetry, the same spectrum is obtained regardless of the polarization. To consider the material dispersions of μc-Si and IZO, we carried out multiple calculations for every wavelength with the corresponding material parameters. The optical absorption spectrum in a wavelength range of 500–1000 nm for the structure obtained by exhaustive-search is shown in Fig. 3(c), with the spectrum for the structure with 4 × 4 superlattice structure shown in Fig. 2(c). The optical absorption spectrum of the solar cell structure obtained by exhaustive-search is much larger than that with the 4 × 4 superlattice structure [see Fig. 2(c)].

In the design of a photonic crystal structure, we should discuss not only the radii of the rods but also other parameters including rod positions and shapes. Here, we adopted sensitivity analysis [13], [14] to finely modulate the photonic crystal structure. This method can show the variations of object functions induced by permittivity changes in the design space relatively easily, as mentioned below. By setting both a photonic crystal in the design space and the power absorbed in the photovoltaic material in the object function to find solar cell structures that can realize large optical absorption.

The excitation source is placed on the excitation plane shown in Fig. 4. F, which is the power that passes through the observation plane, is set to the object function, defined as:

$$F = \int_S \left(\int_0^T G' dt \right) dS \tag{1}$$

$$G' = E_x H_y - E_y H_x \tag{2}$$

where E_x (E_y) and H_x (H_y) are the x-directional (y-directional) electric and magnetic fields. Here, as mentioned above, F corresponds to the optical absorption in the photovoltaic materials. Design variable p_i, which is assigned to the permittivity in point i of the design plane in a photonic crystal (see Fig. 4), is set to

$$p_i = \begin{cases} 1, & \text{(high permittivity material)} \\ 0, & \text{(low permittivity material).} \end{cases} \tag{3}$$

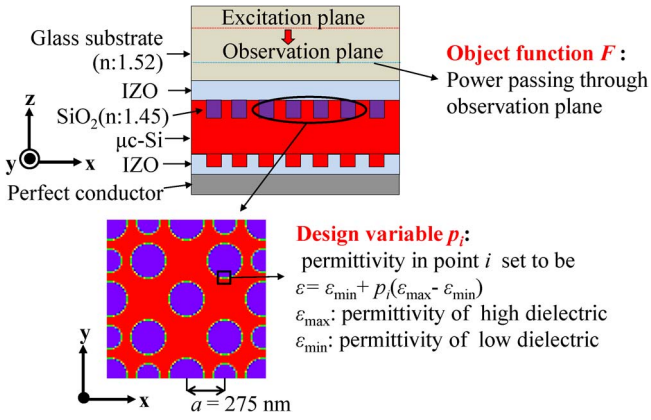

Fig. 4. Two parameters required for structural design using sensitivity analysis.

ε and σ are defined using by p_i as

$$\begin{aligned} \varepsilon &= \varepsilon_{\min} + p_i(\varepsilon_{\max} - \varepsilon_{\min}) \\ \sigma &= \sigma_{\min} + p_i(\sigma_{\max} - \sigma_{\min}) \end{aligned} \tag{4}$$

assuming that permittivity ε and conductivity σ at each point can take an intermediate value between the maximum and minimum of each one.

Next we discuss $\partial F/\partial p_i$. This index represents the variation of object function F when the permittivity of point i in the design plane changes. If this value is found, we can obtain a design rule of the photonic crystal structure. Optical absorption can be enhanced by increasing the permittivity of the point if $\partial F/\partial p_i > 0$ or by decreasing the permittivity of the point if $\partial F/\partial p_i < 0$. $\partial F/\partial p_i$ can be derived by performing the FDTD calculation twice (calculation details are shown in the Appendix) [13], [14].

We selected the structure obtained by exhaustive-search [see Fig. 3(b)] as the initial structure and carried out sensitivity analysis for a vertically incident, both x- and y- polarized pulses (center wavelength of each pulse is 800 nm and FWHM is about 300 nm) as an excitation source. We calculated $\partial F/\partial p_i$ for this structure, and the obtained 2D plot of $\partial F/\partial p_i$ (the superposition of the results for both polarizations) is shown in Fig. 5(a). This shows the positions in which permittivity should be varied. We gave the permittivity change of each point by an amount proportional to $\partial F/\partial p_i$ that was obtained by sensitivity analysis at each step, based on the following equations:

$$\begin{aligned} p_i' &= p_i + \alpha \frac{\partial F}{\partial p_i} \\ \alpha &= 0.05 \left| \frac{\partial F}{\partial p_i} \right|_{\max}^{-1}. \end{aligned} \tag{5}$$

We set the maximum variation of p_i to 0.05 at each step, and the range of p_i between 0 and 1. Then, we calculated $\partial F/\partial p_i$ for the updated structure 900 times. The relative absorptivity against the initial structure for the incident pulse is shown in Fig. 5(b). We found that the pulse absorption increased as we repeated the calculation. The insets show the permittivity distributions of the photonic crystal patterns obtained by repeating the procedure 50, 100, 200, and 900 times, called step 50, step 100, step 200, and step 900, respectively. At steps 50 and 100, some areas have an intermediate value between the permittivity of Si and that of SiO_2 (the green and yellow regions), but such areas become smaller at step 200. At step 900, such areas are much smaller, and almost all areas are occupied by Si or SiO_2.

We calculated the optical absorption spectrum with step 900, and the result is shown in Fig. 6. The optical absorption spectrum of the structure shown in Fig. 2(c) is also shown. This result shows that step 900 has larger optical absorption around a wavelength of 800 nm.

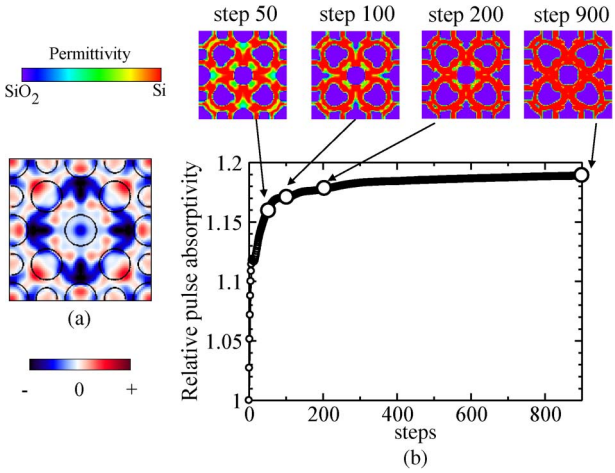

Fig. 5. (a) Spatial distribution of $\partial F/\partial p_i$ for 4 $\times$ 4 period superlattice obtained by exhaustive-search. Optical absorption can be enhanced by increasing permittivity if $\partial F/\partial p_i > 0$ (red), or by decreasing permittivity if $\partial F/\partial p_i < 0$ (blue). (b) Change of pulse absorptivity when we repeated structural design using sensitivity analysis and schematic of photonic superlattice obtained when we repeated structural design using sensitivity analysis. Insets show structures obtained by repeating calculations 50, 100, 200, and 900 times.

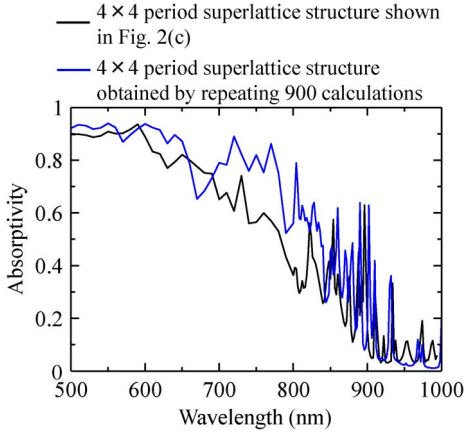

Fig. 6. Optical absorption spectra obtained by FDTD calculations for 4 $\times$ 4 period superlattice shown in Fig. 2(c) and superlattice at step 900.

To evaluate these results quantitatively, we calculated the average optical absorptivity weighted by solar spectral irradiance in a wavelength range of 500–1000 nm:

$$\frac{\int_{500\,\mathrm{nm}}^{1000\,\mathrm{nm}} I(\lambda)S(\lambda)\lambda d\lambda}{\int_{500\,\mathrm{nm}}^{1000\,\mathrm{nm}} S(\lambda)\lambda d\lambda} \tag{6}$$

where $I(\lambda)$ and $S(\lambda)$ are the dependences of the optical absorptivity on the wavelengths and the solar spectral irradiance (air mass 1.5). Using Eq. (6), the average optical absorptivity of the structure obtained by the 900 calculations was 65.1% in a wavelength range of 500–1000 nm. We also investigated the absorption for the incline angle incidences for the 4 $\times$ 4 period superlattices shown in Fig. 2(c) and the step 900 structure. We calculated the absorption spectra for various

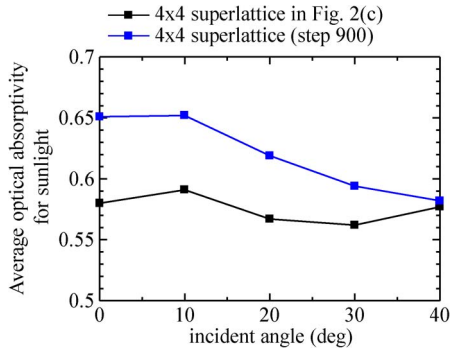

Fig. 7. Average optical absorptivity for various angle incidents.

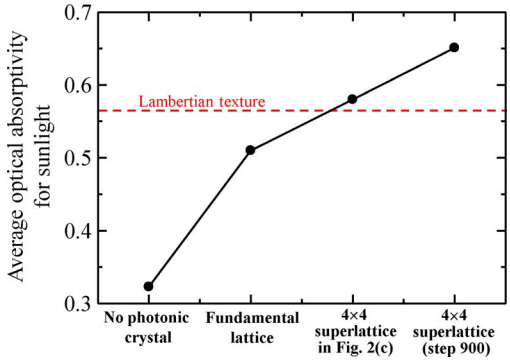

Fig. 8. Average optical absorptivity for sunlight for no photonic crystal, fundamental lattice, 4 $\times$ 4 period superlattice shown in Fig. 2(c), and structure with step 900. Red dashes show the average optical absorptivity for Lambertian texture.

angles. Fig. 7 shows the average optical absorptivity defined as Eq. (6). This result indicates that the step 900 structure has larger optical absorption than the structure in Ref. [15] in the incline angle range of 0–40 degree, although the average optical absorptivity of the step 900 structure decreases gradually as the incline angle increases.

Fig. 8 summarizes average optical absorptivity for sunlight for the structure without photonic crystal and with a fundamental lattice photonic crystal with all rod radii 0.4a [15], the 4 $\times$ 4 superlattice in Ref. [15], and the step 900 structure. In addition, we calculated the optical absorption of the Lambertian textured structure [1] with μc-Si thickness of 400 nm and obtained the average optical absorptivity that is also shown in the figure. From Fig. 5, we realized that the solar cell structure at step 900 had more optical absorption than that with the photonic crystal structure shown in Fig. 2(c) and more than twice as much optical absorption as that without photonic crystal. Moreover, the solar cell structure with the photonic crystal structure at step 900 had more optical absorption than the Lambertian textured structure. By employing pulses with other wavelength or multiple wavelength pulses for the design, structures with more optical absorption can be enhanced.

Finally, we discuss the origin of the larger optical absorption in the step 900 structure. Fig. 9 shows the distribution of the Γ points in the reciprocal space when a photonic superlattice is introduced with the air and glass light cones in the frequency of 0.34 c/a (808 nm). From this figure, not only the original Γ point $((k_x, k_y) = (0, 0))$, but also other Γ points exist in the light cone when using 4 $\times$ 4 superlattice. These components may induce radiation in oblique directions. We calculated $Q_\perp$ and Q_{angle} of the band-edge modes between 650–800 nm, which represent the Q-factor with the coupling of a photonic band-edge mode to the vertical direction and to the oblique directions, and found that Q_{angle} in the step 900 structure is generally larger than that in the superlattice in Ref. [15]. This indicates that the loss in the oblique directions is suppressed in the step 900 structure, and optical absorption is enhanced. Detailed analysis will be discussed in a separate publication.

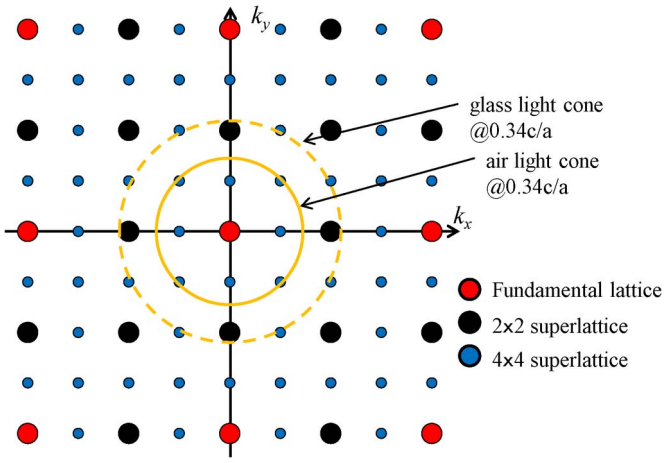

Fig. 9. Distribution of Γ points of superlattices and light cones.

In summary, we explored photonic crystal structures with larger optical absorption in many wavelengths by the following two steps. First, we chose a structure with the largest absorption within the investigated patterns by exhaustive-search. Then, by repeating sensitivity analysis with the structure, we obtained a photonic crystal structure with larger optical absorption. Our final solar cell structure had more than twice as much optical absorption as that without a photonic crystal in a wavelength range of 500–1000 nm. From this result, we showed that the combination of the two steps was useful for designing solar cells with photonic crystals.

Appendix
Detailed calculation method of $\partial F/\partial p_i$

By Eq. (1), $\partial F/\partial p_i$ is written as

$$\frac{\partial F}{\partial p_i} = \int_S \left(\int_0^T \frac{\partial G'}{\partial \boldsymbol{E}} \frac{\partial \boldsymbol{E}}{\partial p_i} dt \right) dS. \tag{A1}$$

Here, $\partial G'/\partial \boldsymbol{E}$ represents a variation of G' when the electric field intensity on the observation plane changes and is written as

$$\frac{\partial G'}{\partial \boldsymbol{E}} = \left(\frac{\partial G'}{\partial E_x}, \frac{\partial G'}{\partial E_y}, \frac{\partial G'}{\partial E_z} \right) = (H_y, -H_x, 0). \tag{A2}$$

$\partial \boldsymbol{E}/\partial p_i$ is a variation of the electric field on the observation plane when the permittivity in point i changes, and it is typically difficult to directly obtain this value. To obtain $\partial F/\partial p_i$, we replace the surface integral of Eq. (1) with the volume integral and rewrite it:

$$F = \int_V \left(\int_0^T G dt \right) dV \tag{A3}$$

$$G = \begin{cases} E_x H_y - E_y H_x, & \text{(on observation plane } S\text{)} \\ 0, & \text{(except above).} \end{cases} \tag{A4}$$

From Maxwell's Equations,

$$\varepsilon \frac{\partial^2 \boldsymbol{E}}{\partial t^2} + \sigma \frac{\partial \boldsymbol{E}}{\partial t} + \nabla \times \left(\frac{1}{\mu} \nabla \times \boldsymbol{E} \right) = \boldsymbol{0} \tag{A5}$$

should be satisfied in the entire calculation space (excitation source is ignored). Using Eq. (A5), Eq. (A3) can be changed to

$$F = \int_V \left[\int_0^T G - \hat{\boldsymbol{E}} \cdot \left\{ \varepsilon \frac{\partial^2 \boldsymbol{E}}{\partial t^2} + \sigma \frac{\partial \boldsymbol{E}}{\partial t} + \nabla \times \left(\frac{1}{\mu} \nabla \times \boldsymbol{E} \right) \right\} dt \right] dV. \tag{A6}$$

This process corresponds to adding zero to the right side of Eq. (A3). $\hat{\boldsymbol{E}}$ is called an adjoint variable vector, and Eq. (A6) is satisfied regardless of $\hat{\boldsymbol{E}}$ because of Eq. (A5).

Assuming $\boldsymbol{E}|_{t=0} = \boldsymbol{0}$, $\hat{\boldsymbol{E}}|_{t=T} = \boldsymbol{0}$ and $(\partial \hat{\boldsymbol{E}}/\partial \hat{\boldsymbol{t}})|_{t=T} = \boldsymbol{0}$ as boundary conditions, Eq. (A6) is derived by

$$\frac{\partial F}{\partial p_i} = \int_V \left[\int_0^T \left[\frac{\partial \boldsymbol{E}}{\partial p_i} \cdot \left\{ \frac{\partial G}{\partial \boldsymbol{E}} - \left\{ \varepsilon \frac{\partial^2}{\partial t^2} - \sigma \frac{\partial}{\partial t} + \nabla \times \left(\frac{1}{\mu} \nabla \times \right) \right\} \hat{\boldsymbol{E}} \right\} - \hat{\boldsymbol{E}} \cdot \left\{ \frac{\partial \varepsilon}{\partial p_i} \frac{\partial^2 \boldsymbol{E}}{\partial t^2} + \frac{\partial \sigma}{\partial p_i} \frac{\partial \boldsymbol{E}}{\partial t} \right\} \right] dt \right] dV. \tag{A7}$$

Now, we assume that $\hat{\boldsymbol{E}}$ satisfies

$$\left\{ \varepsilon \frac{\partial^2}{\partial t^2} - \sigma \frac{\partial}{\partial t} + \nabla \times \left(\frac{1}{\mu} \nabla \times \right) \right\} \hat{\boldsymbol{E}} = \frac{\partial G}{\partial \boldsymbol{E}}$$
$$\hat{\boldsymbol{E}}|_{t=T} = \boldsymbol{0}, \quad \frac{\partial \hat{\boldsymbol{E}}}{\partial t}|_{t=T} = \boldsymbol{0}. \tag{A8}$$

Then Eq. (A7) is modified to

$$\frac{\partial F}{\partial p_i} = \int_V \left[\int_0^T \left[-\hat{\boldsymbol{E}} \cdot \left\{ \frac{\partial \varepsilon}{\partial p_i} \frac{\partial^2 \boldsymbol{E}}{\partial t^2} + \frac{\partial \sigma}{\partial p_i} \frac{\partial \boldsymbol{E}}{\partial t} \right\} \right] dt \right] dV. \tag{A9}$$

As a result, the term $\partial \boldsymbol{E}/dp_i$ can be eliminated. Comparing Eq. (A8) with the normal Maxwell's Equation shown below

$$\left\{ \varepsilon \frac{\partial^2}{\partial t^2} + \sigma \frac{\partial}{\partial t} + \nabla \times \left(\frac{1}{\mu} \nabla \times \right) \right\} \boldsymbol{E} = -\frac{\partial \boldsymbol{J}}{\partial t}. \tag{A10}$$

Eq. (A8) resembles Maxwell's Equation, but it should be solved in the backward time direction. The boundary condition is $\hat{\boldsymbol{E}}|_{t=T} = \boldsymbol{0}$, which means that $\hat{\boldsymbol{E}}$ equals zero at the final value of time $(t = T)$. We obtained $\hat{\boldsymbol{E}}$ by solving the Maxwell's Equation whose direction of time is replaced in the backward time direction from the final value. This process corresponds to analyzing Maxwell's Equations whose initial value of $\hat{\boldsymbol{E}}$ is zero and arranging the results in the backward time direction. As an excitation source, the current source must be chosen that satisfies

$$\frac{\partial \boldsymbol{J}}{\partial t} = -\frac{\partial G}{\partial \boldsymbol{E}}. \tag{A11}$$

References

[1] E. Yablonovitch and G. D. Cody, "Intensity enhancement in textured optical sheets for solar cells," *IEEE Trans. Electron. Devices*, vol. ED-29, no. 2, pp. 300–305, Feb. 1982.

[2] X. Sheng, S. G. Johnson, J. Michel, and L. C. Kimering, "Optimization-based design of surface textures for thin-film Si solar cells," *Opt. Exp.*, vol. 19, no. S4, pp. A841–A850, Jul. 2011.

[3] H. Sai, K. Saito, N. Hozuki, and M. Kondo, "Relationship between the cell thickness and the optimum period of textured back reflectors in thin-film microcrystalline silicon solar cells," *Appl. Phys. Lett.*, vol. 102, no. 5, p. 053509, Feb. 2013.

[4] W. H. Koo, W. Youn, P. Zhu, X. H. Li, N. Tansu, and F. So, "Light extraction of organic light emitting diodes by defective hexagonal-close-packed array," *Adv. Funct. Mater.*, vol. 22, no. 16, pp. 3454–3459, Aug. 2012.

[5] X. H. Li, R. Song, Y. K. Ee, J. F. Gilchrist, and N. Tansu, "Light extraction efficiency and radiation patterns of III-nitride light-emitting diodes with colloidal microlens arrays with various aspect ratios," *IEEE Photon. J.*, vol. 3, no. 3, pp. 489–499, Jun. 2011.
[6] J. Q. Xi, M. F. Schubert, J. K. Kim, E. F. Schubert, M. Chen, S. Y. Lin, W. Liu, and J. A. Smart, "Optical thin-film materials with low refractive index for broadband elimination of Fresnel reflection," *Nature Photon.*, vol. 1, pp. 176–179, 2007.
[7] S. Noda, A. Chutinan, and M. Imada, "Trapping and emission of photons by a single defect in a photonic bandgap structure," *Nature*, vol. 407, pp. 608–610, 2000.
[8] E. Yablonovitch, "Inhibited spontaneous emission in solid-state physics and electronics," *Phys. Rev. Lett.*, vol. 58, no. 20, pp. 2059–2062, 1987.
[9] M. Florescu, H. Lee, I. Puscasu, M. Puscasu, M. Pralle, L. Florescu, D. Z. Ting, and J. P. Dowling, "Improving solar cell efficiency using photonic band-gap materials," *Solar Energy Mater. Solar Cells*, vol. 91, pp. 1599–1610, 2007.
[10] M. D. Zoysa, T. Asano, K. Mochizuki, A. Oskooi, T. Inoue, and S. Noda, "Conversion of broadband to narrowband thermal emission through energy recycling," *Nature Photon.*, vol. 6, pp. 535–539, 2012.
[11] S. Noda, M. Yokoyama, M. Imada, A. Chutinan, and M. Mochizuki, "Polarization control of two-dimensional photonic crystal laser by unit cell structure design," *Science*, vol. 293, no. 5532, pp. 1123–1125, 2001.
[12] K. Sakai, E. Miyai, T. Sakaguchi, D. Ohnishi, T. Okano, and S. Noda, "Lasing band-edge identification for a surface-emitting photonic crystal laser," *IEEE J. Sel. Areas. Commun.*, vol. 23, no. 7, pp. 1335–1340, Jul. 2005.
[13] M. Yokoyama and S. Noda, "Finite-difference time-domain simulation of two-dimensional photonic crystal surface-emitting laser," *Opt. Exp.*, vol. 13, no. 8, pp. 2869–2880, Apr. 2005.
[14] H. Shigeta, M. Fujita, Y. Tanaka, A. Oskooi, H. Ogawa, Y. Tsuda, and S. Noda, "Enhancement of photocurrent in ultrathin active-layer photodetecting devices with photonic crystals," *Appl. Phys. Lett.*, vol. 101, no. 16, p. 161 103, Oct. 2012.
[15] Y. Tanaka, Y. Kawamoto, M. Fujita, and S. Noda, "Enhancement of optical absorption in photovoltaic devices on multiple wavelengths by band-edge effect of photonic crystals," *Opt. Exp.*, vol. 21, no. 17, pp. 20 111–20 118, Aug. 2013.
[16] Y-S. Chung, C. Cheon, I-H. Park, and S-Y. Hahn, "Optimal design method for microwave device using time domain method and design sensitivity analysis—Part II: FDTD case," *IEEE Trans. Magn.*, vol. 37, no. 5, pp. 3255–3259, Sep. 2001.
[17] J. S. Jensen and O. Sigmund, "Topology optimization for nano-photonics," *Laser Photon. Rev.*, vol. 5, no. 2, pp. 308–321, Mar. 2011.
[18] J. Springer, A. Poruba, and M. Vanecek, "Improved three-dimensional optical model for thin-film silicon solar cells," *J. Appl. Phys.*, vol. 96, no. 9, pp. 5329–5337, Nov. 2004.
[19] A. Shah, H. Schade, M. Vanecek, J. Meier, E. Vallet-Sauvain, N. Wyrsch, U. Kroll, C. Droz, and J. Bailat, "Thin film silicon and solar cell technology," *Progr. Photovoltaics: Res. Appl.*, vol. 12, no. 2/3, pp. 113–142, May 2004.